nature energy

ARTICLES

https://doi.org/10.1038/s41560-021-00832-7

Check for updates

# Persistent and partially mobile oxygen vacancies in Li-rich layered oxides

Peter M. Csernica[1], Samanbir S. Kalirai[1,2], William E. Gent[1], Kipil Lim[1,3], Young-Sang Yu[2], Yunzhi Liu[1], Sung-Jin Ahn[4], Emma Kaeli[1], Xin Xu[1], Kevin H. Stone[3], Ann F. Marshall[5], Robert Sinclair[1], David A. Shapiro[2]✉, Michael F. Toney[3,6]✉ and William C. Chueh[1,7]✉

**Increasing the energy density of layered oxide battery electrodes is challenging as accessing high states of delithiation often triggers voltage degradation and oxygen release. Here we utilize transmission-based X-ray absorption spectromicroscopy and ptychography on mechanically cross-sectioned $Li_{1.18-x}Ni_{0.21}Mn_{0.53}Co_{0.08}O_{2-\delta}$ electrodes to quantitatively profile the oxygen deficiency over cycling at the nanoscale. The oxygen deficiency penetrates into the bulk of individual primary particles (~200 nm) and is well-described by oxygen vacancy diffusion. Using an array of characterization techniques, we demonstrate that, surprisingly, bulk oxygen vacancies that persist within the native layered phase are indeed responsible for the observed spectroscopic changes. We additionally show that the arrangement of primary particles within secondary particles (~5 µm) causes considerable heterogeneity in the extent of oxygen release between primary particles. Our work merges an ensemble of length-spanning characterization methods and informs promising approaches to mitigate the deleterious effects of oxygen release in lithium-ion battery electrodes.**

Two of the primary challenges that face the commercialization of lithium- and manganese-rich (LMR) materials are the progressive fading of the discharge voltage over cycling[1–7] and their tendency to release oxygen at high states of delithiation. Although oxygen release in layered oxides has been extensively studied on the first electrochemical cycle, less is known about the process over extended cycling. This is partly because, in contrast to the first cycle, only small quantities of oxygen are released in each subsequent cycle, such that a negligible signal can be detected in electrochemical mass spectrometry studies[8–10]. Additionally, it remains challenging to reconcile nanoscale observations, some of which suggest substantial mass loss and Li depletion coincident with a release of nearly one-fifth of the oxygen[11], with cell-level observations of negligible capacity fade over 100+ cycles[11–13]. Nevertheless, oxygen release during extended cycling has recently been proposed to be the underlying cause of the voltage fade, as it activates lower-voltage redox couples[12,14] and is believed to inevitably cause pernicious phase transitions[7,15]. Therefore, to develop practical strategies to mitigate both oxygen release and voltage decay in LMR materials, several aspects of the oxygen release phenomenon must be clarified.

First, the ability of these materials to transport oxygen at room temperature is uncertain, and thus it is unclear whether the oxygen deficiency is limited to the near-surface (a few nanometres) region[9,16,17] or penetrates into the bulk of primary particles (hundreds of nanometres) after many cycles[11]. Second, owing to a gap in length scales accessed by standard analytical techniques, the influence of microstructure on the heterogeneity of oxygen release has not been assessed. Third, the structural implications of oxygen release during extended cycling remain unclear. The established view, supported primarily from local transmission electron microscopy (TEM) observations[7,15], is that oxygen release is invariably associated with a phase transition to a more transition-metal-rich phase (for example, a spinel or spinel-like phase)[7,15,16,18–21]. However, bulk-sensitive X-ray diffraction studies often do not show the growth of new peaks indicative of a macroscopic phase transformation[2,5], which calls into question whether bulk phase transformations indeed govern the behaviour of LMR layered oxides. Finally, it remains ambiguous whether oxygen release is simply correlated with the commonly observed bulk cation disordering (within the native layered phase)[3,5] or if there exists a mechanistic relationship between the two phenomena.

In this work, we obtained oxidation state maps that span interfaces (~10 nm), primary particles (~200 nm), secondary particles (~5 µm), and the entire electrode thickness (>40 µm) using nanoscale X-ray spectromicroscopy and ptychography on electrodes sectioned by solvent-free ultramicrotomy. These quantitative maps reveal that oxygen originating in the bulk of the primary particles is eventually released over hundreds of cycles at room temperature. The oxygen deficiency profiles suggest that oxygen vacancy diffusion, as opposed to a phase transition, likely governs oxygen release in $Li_{1.18-x}Ni_{0.21}Mn_{0.53}Co_{0.08}O_{2-\delta}$ (LMR-NMC). The existence of bulk oxygen vacancies that persist within the native layered phase was confirmed by additional chemical and structural analysis, which overturns the prevailing view that oxygen release is necessarily accompanied by a phase transition. This result also contradicts the suspicion that oxygen vacancies, if present, will inevitably undergo vacancy condensation and be eliminated from the lattice[11]. Importantly, the existence of bulk oxygen vacancies provides a plausible atomistic explanation that links progressive oxygen release to progressive single-phase cation disordering[3,5], which unifies two

[1]Department of Materials Science and Engineering, Stanford University, Stanford, CA, USA. [2]Advanced Light Source, Lawrence Berkeley National Laboratory, Berkeley, CA, USA. [3]Stanford Synchrotron Radiation Lightsource, SLAC National Accelerator Laboratory, Menlo Park, CA, USA. [4]Energy Lab, Samsung Advanced Institute of Technology, Suwon-si, South Korea. [5]Stanford Nano Shared Facilities, Stanford University, Stanford, CA, USA. [6]Department of Chemical and Biological Engineering, University of Colorado Boulder, Boulder, CO, USA. [7]Stanford Institute for Materials and Energy Sciences, SLAC National Accelerator Laboratory, Menlo Park, CA, USA. ✉e-mail: dashapiro@lbl.gov; Michael.Toney@colorado.edu; wchueh@stanford.edu

previously proposed explanations for the voltage decay. Finally, we reveal that the extent of oxygen release for an individual primary particle depends on the surrounding secondary structure, with those that reside in the interior of large secondary particles being more protected from oxygen release. Together, these results inform new chemical, structural and morphological strategies to prevent oxygen release in layered oxide positive electrodes.

## Cation disordering and reduction over cycling

Uncoated LMR-NMC electrodes were cycled in full cells against graphite (Samsung mini-18650; Methods). Electrodes were harvested at various cycle numbers and assembled into half-cells, where they were cycled once more against Li metal. Figure 1a shows charging and discharging at ~4 mA $g^{-1}$ in a half-cell after up to 500 full cell cycles (Methods). With cycling, the quasi-open-circuit voltage of various redox processes decreased on both charge and discharge, which implies that considerable changes occurred in the bulk of the material[5]. Despite these changes, however, the capacity fade was minimal, as the electrode retained 96% of its initial low-rate discharge capacity (Supplementary Fig. 1). The stable low-rate discharge capacity suggests that the Li content of electrodes discharged at low rate (in a half-cell) is similar regardless of cycle number, which we confirmed directly through inductively coupled plasma mass spectroscopy (ICP-MS; Supplementary Fig. 2).

Rietveld refinement of the synchrotron powder X-ray diffraction (SXRD) patterns reveals that LMR-NMC remains single phase with the $R\bar{3}m$ space group after 500 cycles with no tetrahedral occupancy of the transition metals (TMs) (Fig. 1b and Supplementary Figs. 3–6). The lack of secondary crystallographic phases is also supported by selected area electron diffraction (Supplementary Figure 7) and high-resolution TEM (Supplementary Figures 8 and 9). Interestingly, Rietveld refinement does show that the TM occupancy in the Li layer octahedral sites increases steadily from 2 to 10 at% with cycling (Fig. 1c), consistent with previous reports[5,22].

We additionally probed the spatially averaged electronic structure[23] using transmission-based TM K-edge X-ray absorption spectroscopy (XAS) (Supplementary Figs. 10–12). With cycling, Mn and Co are progressively reduced from their initial $Mn^{4+}$ and $Co^{3+}$ states, whereas Ni remained in its initial $Ni^{2+}$ state (Fig. 1c). Given that the Li content in each sample is approximately identical and that the crystallographic phase of the material is unchanged, we infer from bulk electroneutrality that the spectroscopic changes here correspond to oxygen release[12]. This conclusion is also consistent with the SXRD Rietveld refinements[24] (Supplementary Figs. 3 and 13) and nanoscale oxidation state maps, which are discussed below. Interestingly, the reduction of Mn and Co over cycling can be partially reversed by conducting a low-temperature heat treatment at 150 °C in 100% $O_2$ (Fig. 1c). We discuss this intriguing result in detail later.

The TM oxidation states from XAS were used to estimate the fraction of oxygen release normalized to the oxygen content of the pristine material, ~3.3 at% after the first cycle (which is preceded by formation cycling) and ~6.5 at% after 500 cycles (Supplementary Note 1). The large first-cycle oxygen release is consistent with the findings of previous gas-analysis experiments[16,25,26]. Our XAS results, taken together with our findings from SXRD, reveal that both phenomena previously linked to voltage fade—progressive cation disordering and progressive oxygen release—occur simultaneously over extended cycling. The strong correlation observed here (Fig. 1c) suggests that the two may be mechanistically linked to one another, a point which we return to later.

To map oxygen loss at the nanoscale, we utilized soft X-ray scanning transmission X-ray microscopy (STXM) and X-ray ptychography, the latter with a greater spatial resolving power[27–30], at the Advanced Light Source (ALS). Using these two transmission-based microscopy techniques in spectromicroscopy mode, we probed the TM $L_3$-absorption edges and the oxygen K edge without self-absorption effects. With cycling, Mn and Co reduction were both observed in the averaged (Supplementary Methods) $L_3$-edge spectra, whereas no change was observed at the Ni $L_3$ edge[2] (Supplementary Figs. 14–17). These spectral changes, visible from the difference plots even without quantification (Fig. 1d), are in strong agreement with the TM K-edge spectroscopy results, which provides unambiguous evidence that the *d* electron count increases with cycling.

## Oxidation state heterogeneity within primary particles

As in most layered oxides, primary particles in LMR-NMC exist in secondary particle agglomerates (~5 μm) rather than as isolated particles. To preserve the secondary structure and also make the sample sufficiently transparent to soft X-rays, thin cross-sectional lamellae were prepared by dry mechanical ultramicrotomy (Methods and Supplementary Fig. 18). We first discuss the oxidation state heterogeneity within individual primary particles using X-ray spectroptychography at the Mn $L_3$ edge, which has a resolution of ~5–20 nm (Fig. 2a–c and Supplementary Fig. 19). As expected, the Mn reduction after a single cycle is concentrated near the particle edges, which indicates that oxygen release initiates at the surface of the particles (Fig. 2d and Supplementary Figs. 20 and 21). This observation spatially decouples first-cycle oxygen release, which occurs primarily at the surface, from oxidized lattice oxygen[31], which charge compensates the majority of the capacity in the first-cycle voltage plateau and exists throughout the particle bulk even on the initial cycle[2]. Additionally, there is substantial heterogeneity in the extent of oxygen release between primary particles (Fig. 2b), which we return to later. Finally, the oxygen deficiency that begins on the particle surface progressively enters into the bulk (>100 nm) material over many electrochemical cycles (Fig. 2d). This observation is consistent with previous electron[13] and X-ray[32] microscopy studies that show TM reduction beyond the surface of the LMR particles.

The quantitative nature of the oxidation-state maps of primary particles allows us to directly evaluate two mechanistic possibilities. The first is a single-phase oxygen ambipolar diffusion from the bulk to the particle surface. The second is a two-phase (core–shell) reaction[21,33,34], in which a new phase with a more reduced Mn oxidation state grows inwards from the surface. Figure 2e,g shows three independent fittings to the $Mn^{3+}$ concentration profiles of individual particles for each of the two models (Supplementary Note 2). The fits that utilize a two-phase reaction are poor, as a depth-averaged core–shell model predicts a constant $Mn^{3+}$ concentration in the shell, which is not observed experimentally. Conversely, the individual particle fits that utilize the vacancy diffusion model describe the data reasonably well (Supplementary Fig. 22), which suggests that oxygen chemical diffusion governs the bulk oxygen release in LMR-NMC.

Quantitatively, the fitting (Supplementary Note 2) gives room-temperature oxygen chemical diffusivities ($D_O$) within an order of magnitude of $10^{-17}$ $cm^2$ $s^{-1}$ in the delithiated state, where oxygen is known to be the most mobile[35,36]. This room-temperature oxygen chemical diffusion coefficient, although large enough to cause bulk oxygen depletion over extended cycling, is six to seven orders of magnitude lower than those of some fast oxygen-ion-conducting perovskite oxides[37–40]. Several factors may contribute to oxygen transport in LMR-NMC. As LMR-NMC is known to have oxidized oxygen species at high extents of delithiation (such as molecular $O_2$, $O_2^{2-}$ or $O^-$) (refs [2,41]), the diffusing species may, in fact, be a less ionized oxygen, which could be more mobile[42,43] than $O^{2-}$. Extended defects, such as dislocations, may also contribute[44,45]. We note that, although fitting with a constant oxygen chemical diffusivity gives good fits to the data, the true chemical diffusivity is probably not constant during cycling due to progressive changes in the material

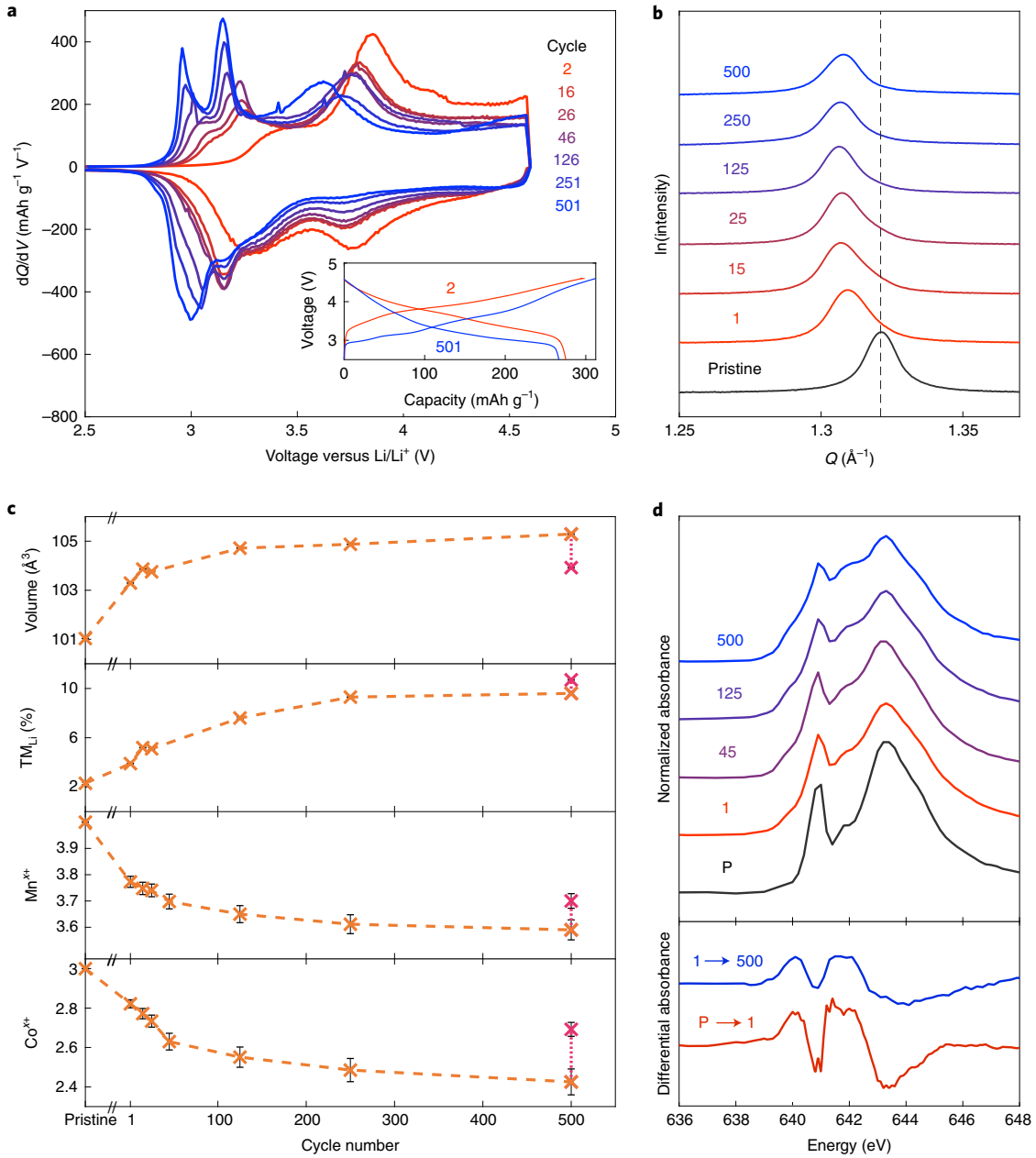


**Fig. 1 | Electrochemical voltage depression linked to cation disordering and TM reduction. a**, Electrochemical differential capacity plots taken at ~4 mA $g^{-1}$. Inset: the discharge capacity remains at ~96% of its initial value even after 500 cycles. **b**, The (003) peak plotted on a logarithmic scale after varying numbers of cycles with an absence of secondary peaks, which indicates that the bulk material remains a single phase on cycling. **c**, The voltage depression on electrochemical cycling is correlated with an increase in the unit cell volume, an increase in the TM occupancy in the Li layer ($TM_{Li}$), and the reduction of the average TM oxidation state ($Co^{x+}$ and $Mn^{x+}$). Error bars are from a Rietveld refinement (Supplementary Fig. 3) and the uncertainty in the edge position versus the oxidation state slope (Supplementary Fig. 11). The TM reduction and lattice volume expansion that occur over cycling can be partially reversed by annealing the cycled electrode at 150 °C (red). **d**, Transmission-based Mn $L_3$-edge spectra obtained through STXM showing considerable changes over 500 cycles (top). The differential spectra (bottom) reveal that a similar change takes place between the 1st and 500th cycle as that which occurs between the pristine (P) material and the 1st cycle.

structure. For completeness, we also performed STXM imaging on dispersed[2] (rather than cross-sectioned) samples, which are consistent with the conclusion of bulk oxygen release (Supplementary Figs. 16 and 17).

## The existence of bulk oxygen vacancies

Although the spatial analysis of $Mn^{3+}$ concentration suggests oxygen vacancies may be present in the bulk material, proof of this remains lacking because neither XAS nor SXRD can directly resolve the anion sublattice. Given that LMR-NMC remains single phase over cycling, we consider two structural models[24,46] for the electrode after 500 cycles (Fig. 3a). The first involves an anion sublattice with vacancies that persist over many cycles, which we refer to as the oxygen vacancy structure ($[Li_{1.18}TM_{0.82}]$ $[O_{1.87}\square_{0.13}]$, where the first and second brackets define the cation and anion sublattices, respectively, and $\square$ represents a vacancy). Here, the point defect reaction

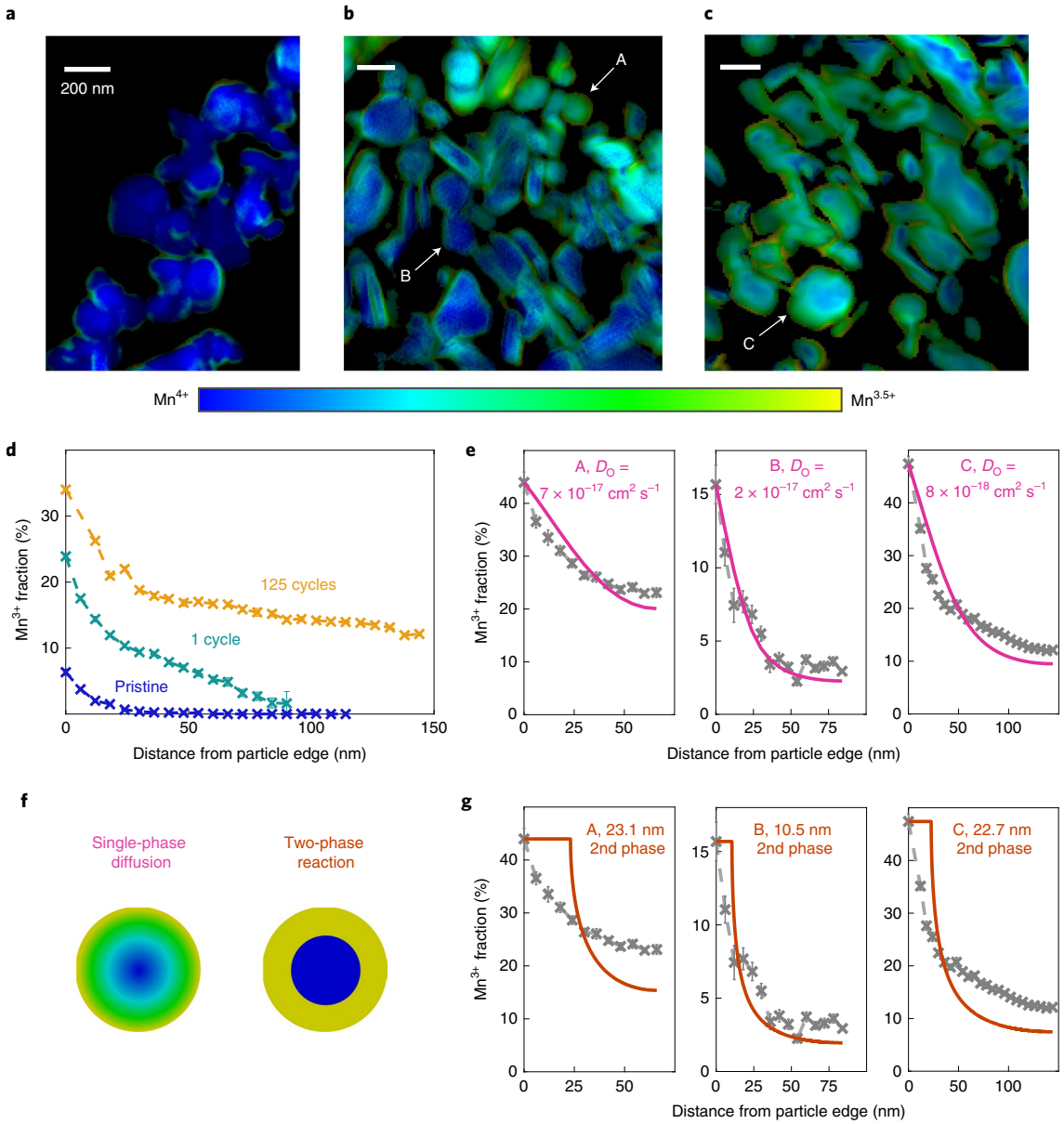


**Fig. 2 | Spatial dependence of the Mn oxidation state within primary particles. a–c**, X-ray ptychography images of the pristine material (**a**) and the material after 1 cycle (**b**) and 125 cycles (**c**). Scale bars, 200 nm. **d**, The $Mn^{3+}$ content as a function of distance from the particle edge. **e**, The $Mn^{3+}$ spatial distribution in selected particles A–C (with minimal particle overlap; Supplementary Note 2) fit with a diffusion profile and an individual chemical diffusion coefficient. The results suggest an overall oxygen chemical diffusion coefficient of ~$10^{-17}$ $cm^2$ $s^{-1}$. **f**, Schematic illustration of two possible mechanisms, single-phase diffusion (left) (**e**) and two-phase reaction (right) (**g**), that can give rise to a $Mn^{3+}$ concentration that is lower in the bulk than on the surface. **g**, The $Mn^{3+}$ spatial distribution in individual particles A–C fit with a two-phase core–shell model (Supplementary Note 2). The fits using this model are qualitatively and quantitatively poor. Error bars are based on the weighted standard error of the $Mn^{3+}$ concentration of the pixels that contribute to each data point.

that governs the changes over cycling in the lithiated material can be written in Kröger–Vink notation as:

$$4TM_{TM}^{\times} + 2O_O^{\times} \rightarrow 2V_O^{\cdot\cdot} + 4TM_{TM}' + O_2(g) \quad (1)$$

The second structural model involves a fully occupied anion sublattice, referred to as the densified structure ($[Li_{1.06}TM_{0.94}]$ $[O_2]$), whereby the evolved oxygen causes TMs at the surface to back diffuse into the bulk[19,21,47–49]. The analogous point defect reaction can be written as:

$$3TM_{TM}^{\times} + 2Li_{Li}^{\times} + 2O_O^{\times} \rightarrow 2TM_{TM}' + TM_{Li}^{\cdot\cdot} + 2Li + O_2(g) \quad (2)$$

These two structure models are indistinguishable using XAS, as both models can explain a reduction in the average TM oxidation state (Fig. 3a). They are also nearly indistinguishable with neutron diffraction (Supplementary Fig. 23) or SXRD[24,46] (Supplementary Fig. 24).

Crucially, the predominant difference between the two structure models is that the densified structure has a considerably lower Li to TM elemental ratio (Li:TM) of 1.12, whereas the oxygen vacancy structure has a Li:TM of 1.44 (Supplementary Note 3). Figure 3b shows that, consistent with the meagre capacity fade observed both here and elsewhere[11–13], the Li:TM of the electrodes discharged to and held at 2.5 V versus $Li/Li^+$ is nearly constant with cycling.

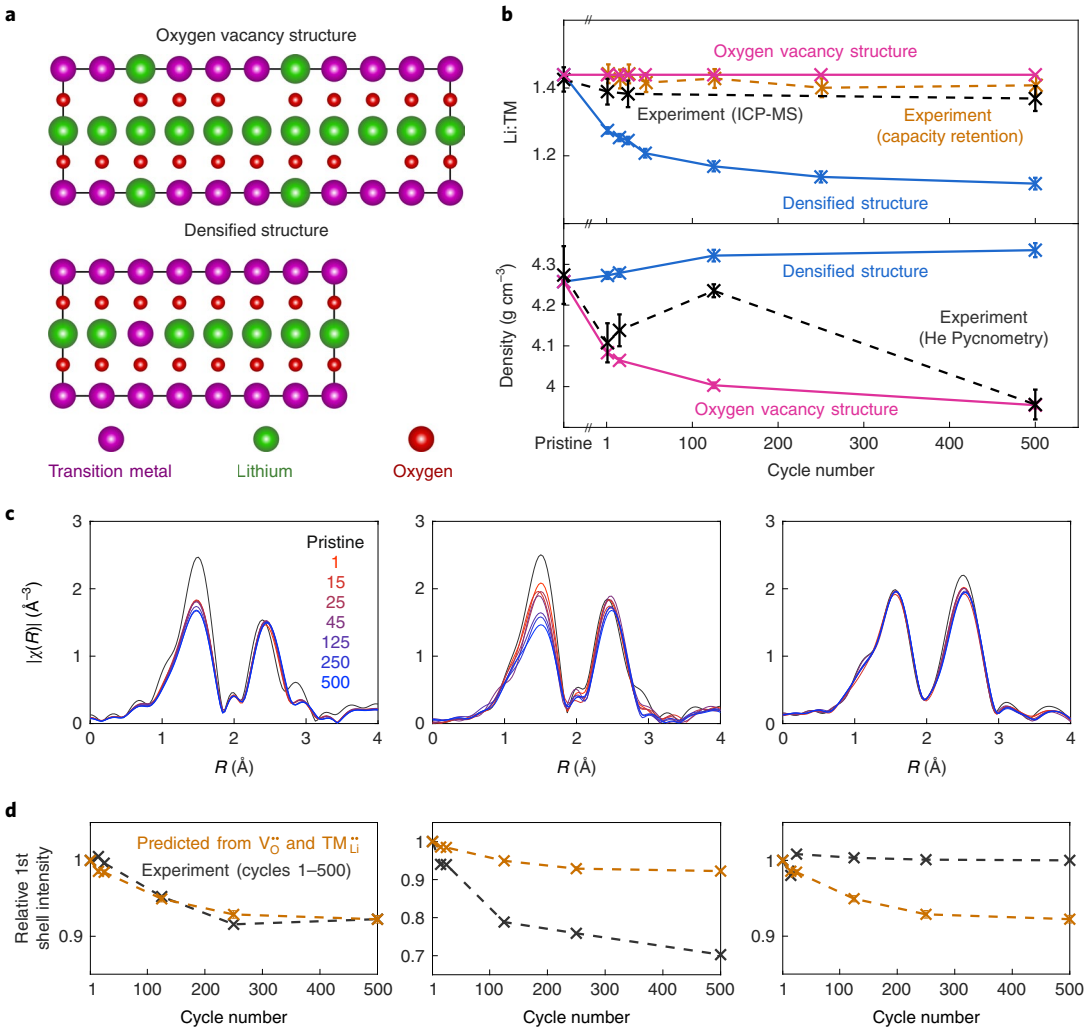


**Fig. 3 | Structural consequences of oxygen release. a**, Graphical depiction of the two possible structures after 500 cycles, the oxygen vacancy structure (top) and the densification structure (bottom), as discussed in the text. The initial structure (not shown) is identical to the vacancy structure in this illustration, but with a full oxygen sublattice. Both structures depicted here would have an identical average TM oxidation state of 2.75+. **b**, ICP-MS, capacity retention and helium pycnometry density measurements (dashed lines). The pink and blue lines represent the expected measurement values if all of the oxygen release was accompanied by the formation of oxygen vacancies or densification, respectively. All three experimental measurements indicate that the majority of the oxygen release causes the formation of oxygen vacancies. The ICP-MS and pycnometry error bars are based on the standard error of repeat measurements. Capacity retention error bars are based on an estimated 5 mAh g$^{-1}$ uncertainty in discharge capacity. Error bars for the structure models are propagated from the uncertainty in the edge position versus oxidation state slope (Supplementary Fig. 11). **c**, EXAFS data at the TM K edge as a function of cycle number showing a decrease in the first-shell scattering intensity with cycling for Mn (left) and Co (centre), but not for Ni (right). **d**, A quantitative comparison of the relative changes in first-shell scattering intensity (approximated by the maximum value of $|\chi(R)|$) at the Mn (left), Co (centre) and Ni (right) K edges with those from the presence of only the $V_O^{\bullet\bullet}$ and $TM_{Li}^{\bullet\bullet\bullet}$ defects. Error bars in the predicted values are propagated from uncertainty in the $V_O^{\bullet\bullet}$ and $TM_{Li}^{\bullet\bullet\bullet}$ concentrations.

This indicates that bulk densification is only a minor contributor (~15% if the entire decrease in Li:TM and electrochemical capacity is due to densification) to the structure of the cycled material. We note that, although the cathode electrolyte interphase may contribute to the ICP-MS signal, the cathode electrolyte interphase would have to contain 22.5% of the Li content of LMR-NMC (after 500 cycles, discharged in a half-cell) and no TMs to explain the ICP-MS results with the densified structure. As a recent cryogenic electron microscopy study showed that the cathode electrolyte interphase on Li-rich materials is essentially non-existent[50], we therefore conclude that, contrary to earlier reports[7,46,47], the bulk oxygen vacancy structure is far more likely to explain both the nearly constant Li:TM over extended cycling and the stable electrochemical capacity (Supplementary Note 4).

The material density also contrasts between the two structural models, with the predicted densities differing by nearly 10% after 500 cycles (Supplementary Note 5). Therefore, we utilized helium gas pycnometry, which has been used to measure cation vacancy concentrations in layered oxides[51], to determine the density of LMR-NMC with cycling. The experimental results agree reasonably well with the density changes predicted by the oxygen vacancy structure model, which provides more support for the existence of oxygen vacancies (Fig. 3b). We note that the presence of closed pores may complicate the interpretation of the pycnometry measurement, a point that is discussed thoroughly in Supplementary Note 6 (also see Supplementary Figs. 25–27).

As a final piece of evidence, we return to the oxidation of TMs on annealing the cycled material (Fig. 1c and Supplementary Fig. 28),

a similar experiment to those conducted in several recent works[45,52] (Supplementary Note 7). In addition to TM K-edge XAS, evidence for TM oxidation includes TM K-edge extended X-ray absorption fine structure (EXAFS) data, Rietveld refinement and electrochemical analysis (Supplementary Figs. 3 and 29–31). The TM oxidation during annealing could come from a change in either the Li or O stoichiometry. If the densified structure were operative before the annealing process, an increase in the oxygen stoichiometry would have to proceed via the insertion of oxygen interstitials:

$$4TM'_{TM} + O_2(g) \rightarrow 4TM^{\times}_{TM} + 2O''_i \quad (3)$$

In addition to being intuitively unlikely, the insertion of oxygen interstitials would almost certainly expand the lattice rather than result in the contraction that is experimentally observed. Alternatively, Li could be removed from the structure during annealing via the following reaction, in which Li on the product side is a Li-containing compound (for example, $Li_2O$):

$$2Li^{\times}_{Li} + 2TM'_{TM} \rightarrow 2TM^{\times}_{TM} + 2V'_{Li} + 2Li \quad (4)$$

This process, which represents lithium loss of a slightly less Li-rich (than the pristine material) oxide in the absence of an electrolyte at 150 °C, is also extremely unlikely. We can therefore conclude that the densified structure is a poor explanation for the structure of the material prior to annealing.

Conversely, if the oxygen vacancy structure was operative, an increase in the oxygen stoichiometry could proceed via the refilling of previously formed oxygen vacancies:

$$2V^{\cdot\cdot}_O + 4TM'_{TM} + O_2(g) \rightarrow 4TM^{\times}_{TM} + 2O^{\times}_O \quad (5)$$

Additionally, a decrease in Li stoichiometry may be possible, as oxygen vacancies present before the annealing process could combine with Li vacancies formed via equation (4):

$$TM^{\times}_{TM} + 2V'_{Li} + 2V^{\cdot\cdot}_O \rightarrow TM^{\cdot\cdot}_{Li} \quad (6)$$

Equation (6), although potentially being kinetically inhibited at room temperature, should be thermodynamically favourable, as the elimination of oxygen vacancies would restore undercoordinated TMs to their full coordination[20]. Combining equations (4) and (6) results in a net defect reaction which could cause TM oxidation if oxygen vacancies are present before annealing, in which Li on the product side is a Li-containing compound (for example, $Li_2O$):

$$2Li^{\times}_{Li} + 2TM'_{TM} + 2V^{\cdot\cdot}_O \rightarrow TM^{\times}_{TM} + TM^{\cdot\cdot}_{Li} + 2Li \quad (7)$$

The thermodynamic favourability of equation (6) means equation (7) is a more plausible alternative to equation (4). Thus, regardless of whether a change in the Li or O stoichiometry governs the TM oxidation, the oxygen vacancy structure is more likely to describe the material before annealing.

We emphasize that in the above discussion (summarized in Supplementary Table 1), we are concerned with the structural changes that occur in the bulk of the material rather than in the near-surface region (a few nanometres), as many publications report a densified surface layer that remains nearly the same thickness during cycling[7,19,53,54].

## Oxygen vacancies and the cation sublattice

The existence of bulk oxygen vacancies confirms that single-phase vacancy diffusion is responsible for the $Mn^{3+}$ concentration profiles within primary particles (Fig. 2). This overturns the accepted view that bulk oxygen release kinetics in LMR-NMC are necessarily governed by phase transitions[12]. Furthermore, bulk oxygen vacancies provide an atomistic link between single-phase cation disordering and oxygen release, both of which occur progressively with cycling and have been independently proposed as the reason for the voltage decay[5,12]. Namely, an oxygen vacancy will cause neighbouring TMs to become undercoordinated and therefore more likely to move to alternative lattice sites. We note that this explanation was previously suggested to be responsible for the observed surface densification process[13,17,19,55]. Cation disordering may also promote oxygen vacancy formation by allowing the lattice to more easily accommodate and/or transport an oxygen vacancy. This coupling suggests that the strategic prevention of either of these phenomena may enhance the electrochemical performance in part due to the coupling between them. Indeed, surface modifications designed to prevent oxygen release mitigate both voltage decay and cation disordering[14,15,56,57]. Likewise, modified stacking sequences or large interlayer spacings that restrict TM mobility mitigate both voltage decay[58–60] and oxygen release[60,61].

As a final point of interest, EXAFS data (Fig. 3c) show a decrease in the scattering intensity of the first coordination shell with cycling for both Mn and Co, but not for Ni. This decrease in intensity can originate from the formation of both $V^{\cdot\cdot}_O$ and $TM^{\cdot\cdot}_{Li}$ (Fig. 3d and Supplementary Fig. 32), although disorder in the first-shell M–O bond distances due to the loss of in-plane ordering or the fractional average oxidation states of Mn and Co may also contribute. However, the Ni first-shell scattering intensity remains higher than would be predicted based on a random distribution of both $V^{\cdot\cdot}_O$ and $TM^{\cdot\cdot}_{Li}$. Therefore, we hypothesize that the oxygen vacancies may preferentially form around Mn and Co, the same atoms that undergo TM reduction (Supplementary Note 8). The EXAFS data additionally suggest that if Ni atoms migrate during delithiation, as has been suggested from previous EXAFS data[2], these migrations may be more reversible than those of Mn and Co. We speculate that this may be due to the large change in ionic radius Ni experiences during cycling, as the sites that $Ni^{4+}$ migrates into on delithiation may not be suitable for the $Ni^{2+}$ that forms on lithiation.

## Importance of secondary particle microstructure

Although cross-sectioning the electrode into nominally 80-nm-thick lamellae cuts through secondary particles, some information about the location of a given primary particle within the secondary structure can be inferred. Specifically, large agglomerates in the lamella represent cross-sections that went through the centre of large secondary particles. Smaller agglomerates could either represent a cross-section closer to the secondary particle edge or through the centre of a smaller secondary particle (Supplementary Fig. 18).

Maps of the Mn oxidation state after one cycle were obtained via STXM at the electrode level (~50 × 50 μm; Fig. 4a) as well as that of a single large agglomerate with finer resolution (~5 × 5 μm; Fig. 4b). Figure 4b reveals that the primary particles inside the large agglomerate are substantially more oxidized, and thus release less oxygen, than those outside the agglomerate. Figure 4c quantitatively demonstrates that this trend is preserved even when controlling for the pixel-wise thickness of the primary particle being examined (Supplementary Fig. 33). This implies that even primary particles of identical size will exhibit a degree of oxygen release that is heavily dependent on their location within the secondary structure. Additionally, Fig. 4b shows that within the large agglomerate, primary particles near the exterior are more reduced than those on the interior (Fig. 4b,d and Supplementary Fig. 34). Taken together, these findings reveal that primary particles originating from the interior of large secondary particles release comparably less oxygen. Conversely, primary particles that originate from either the exterior of large secondary particles or from small secondary particles release a relatively large quantity of oxygen. Both of these observations are quantitatively supported by investigation of an ensemble of large agglomerates (Fig. 4a,d and Supplementary Figs. 35–37).

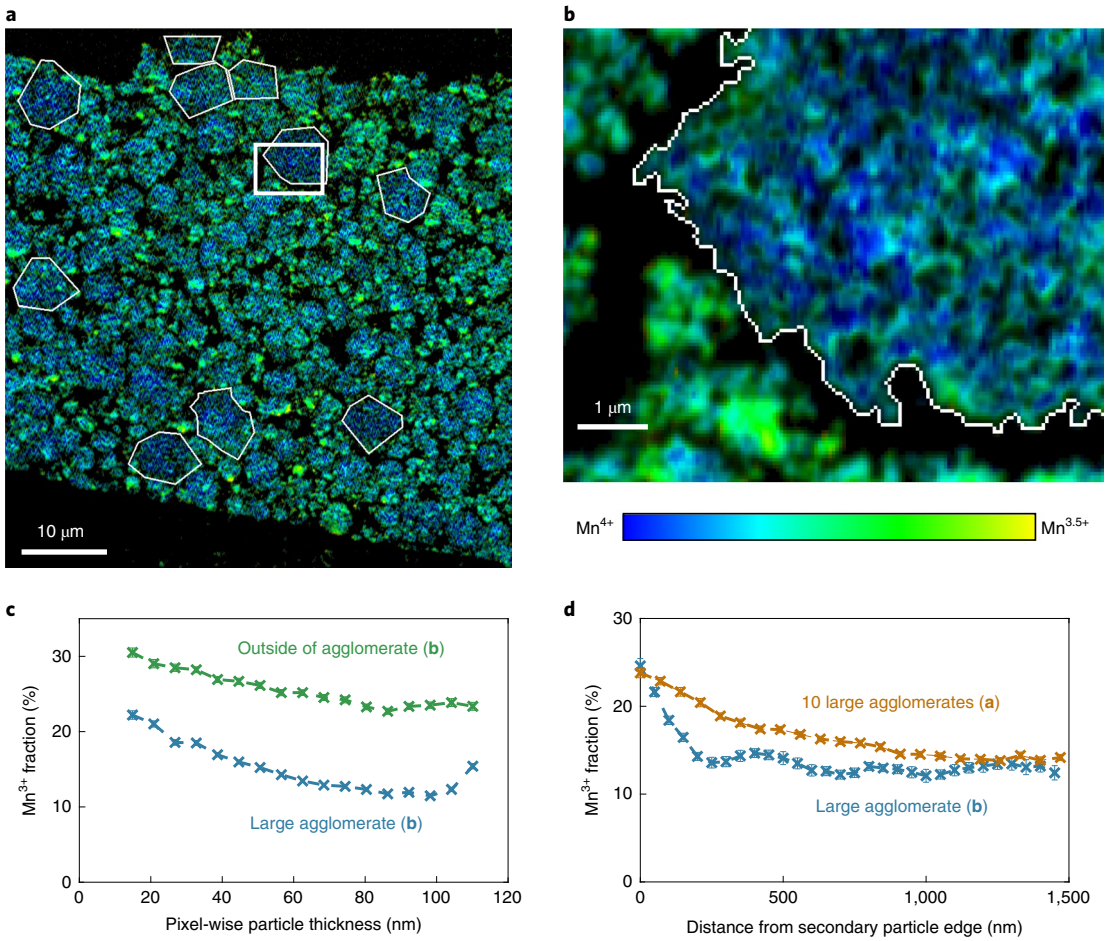


**Fig. 4 | Oxidation state heterogeneity on the secondary particle scale.** The samples shown were taken after one cycle followed by discharging to 2.5 V versus Li/Li$^+$ and holding for ~6 h. **a**, Image with a field of view that covers the entire electrode thickness (~40 μm). Ten large agglomerates are outlined in white. **b**, A single large agglomerate (to the right of the image, outlined in white) that is substantially more oxidized than the surrounding areas. This image, taken at finer resolution than that for **a**, corresponds to the region in the thick white rectangle in **a**. **c**, The trend of a relatively more oxidized large agglomerate is maintained even at a fixed particle thickness, which implies that a primary particle of identical size and shape will be more oxidized within the large agglomerate than outside it. **d**, The primary particles at the exterior of large agglomerates are more reduced than the primary particles in the interior. Error bars are based on the weighted standard error of the $Mn^{3+}$ concentration of the pixels that contribute to each data point.

Interestingly, the fact that the $Mn^{3+}$ distribution in each individual primary particle (Fig. 2a–c) is nearly radial indicates that each primary particle releases oxygen from its surface. Therefore, the observed heterogeneity cannot be explained by differences in the effective oxygen diffusion length among primary particles, as would occur if oxygen release occurred entirely from the secondary particle surface (Supplementary Fig. 38). Although the fundamental reason for the heterogeneity is still under investigation, one possibility is that stress build-up in large secondary particles[62] could modify the local oxygen chemical potential and/or diffusivity. Diminished electrolyte-induced oxygen release for interior primary particles is also possible, although electrolyte penetration into the secondary particle interior may also occur[63,64].

Regardless of the underlying cause, the observed heterogeneity shows that many primary particles must be examined to arrive at robust conclusions (Supplementary Fig. 39). The results additionally suggest that larger secondary particles, with the primary particle size held constant, are expected to exhibit less oxygen release and possibly greater voltage retention. Although this improvement may come at the expense of usable capacity and/or rate capability, spectromicroscopy analysis of delithiated samples suggests that large secondary particles may achieve Li contents comparable to those of smaller secondary particles (Supplementary Fig. 40). Previous work also suggests that the primary particle size may be a more important factor in determining the achievable capacity[63,65]. The possibility of cycling a similar quantity of Li while simultaneously mitigating oxygen release advocates for the exploration of larger LMR-NMC secondary particles.

## Spectroscopic analysis of the delithiated state

Although the Mn $L_3$-edge XAS shows a progressive reduction with cycling in the discharged state, all the LMR-NMC electrodes charged to 4.6 V exhibited a uniform $Mn^{4+}$ oxidation state, even after 500 cycles (Supplementary Fig. 41). This finding verifies the emergence of a reversible $Mn^{3/4+}$ redox couple on cycling[12,16] and further confirms that the bulk Mn reduction observed in the discharged state cannot be due to an electrochemically inactive second phase.

Conversely, oxidation state maps at the Ni $L_3$ edge show the opposite behaviour. Although the Ni oxidation state remains uniform in the discharged electrodes with cycling (Supplementary Figs. 42 and 43), it is heterogeneous in the charged electrodes (Fig. 5). Specifically, Fig. 5d shows that thicker regions reach a higher oxidation state than that of thinner regions[2]. This heterogeneity is probably not due to a sluggish Li$^+$ transport, both because of the

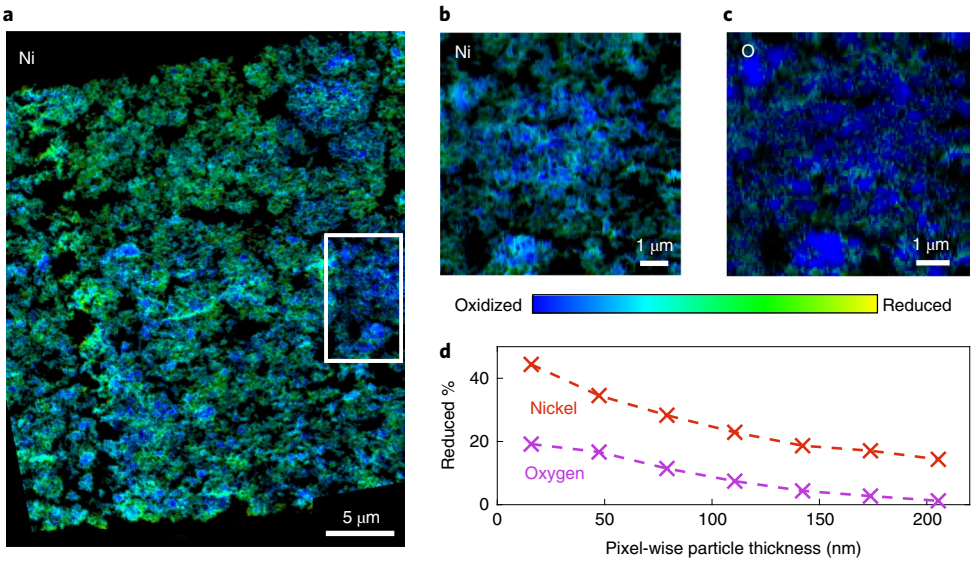


**Fig. 5 | Oxidation state heterogeneity in the charged state.** The samples in this figure were taken after 125 cycles followed by charging to 4.6 V versus Li/Li$^+$ and holding for ~6 h. **a**, Distribution of the Ni oxidation state with a field of view that covers the entire electrode thickness. The area in the white boxed region was imaged a second time with a finer energy resolution, as shown in **b** and **c**. **b**, Distribution of the Ni oxidation state in a large secondary particle. **c**, Distribution of the O oxidation state in a large secondary particle. **d**, Fraction of the reduced component (Supplementary Fig. 42) present as a function of particle thickness for **b** and **c**. The results indicate that the surface of the material is not able to achieve as high an oxidation state as that of the bulk. Error bars are based on the weighted standard error of the $Mn^{3+}$ concentration of the pixels that contribute to each data point.

long constant voltage hold and the fact that thicker regions would be expected to be less oxidized if transport were limiting. Instead, the lower oxidation state of the thinner regions may be due to the fact that these regions have more reduced Mn in the discharged state (Figs. 2d and 4c). This allows Mn to compensate more charge during delithiation, which requires less charge compensation from Ni. Additionally, it is known that the atomic structure at the surface of the particle (~5 nm) reconstructs due to interactions with the electrolyte[54]. This modified surface structure may not cycle as much Li and is generally more reduced than that of the bulk material[54], which may also contribute to the observed thickness dependence.

Interestingly, the O K-edge spectra, like the Ni $L_3$-edge spectra, are uniform in the discharged state (Supplementary Figs. 42 and 44), but exhibit heterogeneity at 4.6 V (Fig. 5c). As shown in Fig. 5d, the O and Ni oxidation states exhibit a similar dependence on particle thickness, probably for the same reasons as described above. The considerable amount of Ni and O oxidation observed[66], particularly for thicker regions where the LMR-NMC bulk is responsible for the majority of the signal, indicates that the existence of bulk oxygen vacancies does not inhibit the redox of either of these elements. This observation is consistent with the negligible capacity fade after 500 cycles.

## Implications for oxygen release mitigation

Substantial efforts have been devoted to the mitigation of oxygen release in layered oxide positive electrodes. By a large margin, the most common approach to resolving this issue is to apply surface treatments to the electrodes[14,15,56,57,67,68]. However, additional approaches should also be considered, particularly because they could work synergistically with an appropriate surface coating. Our results, obtained from an industrially relevant LMR-NMC material, suggest several additional strategies that have not been adequately examined. First, chemical or structural modifications, which can decrease the oxygen chemical diffusivity, a property that is crucial but hardly understood[49] in Li-ion layered oxides, should be explored. Second, the prevention of cation disordering, which is inhibited in many Na-ion materials due to their large interlayer spacing and unique stacking order[69], is another important strategy that may inhibit the structural changes necessary to accommodate an oxygen vacancy. This route has been shown to successfully mitigate oxygen release in Na-ion materials even when they undergo a phase transition that involves layer sliding[60,61]. Finally, our results suggest that morphological control is a potential chemistry-agnostic method to achieve stability against oxygen release. For LMR oxides specifically, larger secondary particles, with the primary particle size held constant, may mitigate the oxygen release problem and preserve electrochemical capacity[63].

## Conclusions

Using X-ray spectromicroscopy and ptychography, we show that bulk lattice oxygen is released in substantial quantities during extended cycling. The extent of oxygen release for an individual primary particle was found to be highly dependent on its location within the secondary structure, which offers opportunities for morphological mitigation of the oxygen release phenomenon. Although oxygen release is typically associated with a phase transition between two or more phases that each contain a full anion sublattice, we demonstrate here that only a small amount (~15%) of material densification occurs, probably at the very surfaces of the primary particles. Instead, surprisingly, the majority of oxygen release over cycling creates bulk oxygen vacancies, which form and persist within the native layered phase. These vacancies, created at the primary particle surface, enter into the bulk over extended cycling with a fitted oxygen chemical diffusivity of ~$10^{-17}$ $cm^2 s^{-1}$ in the delithiated state. Our observations unify previous observations of TM reduction and single-phase cation disordering and imply that cycling-induced oxygen release can be mitigated via chemical or structural modifications that inhibit the formation and/or transport of oxygen vacancies within the bulk material.

## Methods

**Materials.** The $Li_{1.18}Mn_{0.53}Ni_{0.21}Co_{0.08}O_2$ materials were synthesized as previously reported[2]. In short, a $Mn_{0.53}Ni_{0.21}Co_{0.08}(OH)_2$ precursor powder was synthesized by co-precipitation of stoichiometric quantities of $NiSO_4$, $CoSO_4$ and $MnSO_4$.

The precursor was then mixed with the appropriate amount of $Li_2CO_3$ and calcined at 900 °C for 10 h to obtain a powder of the target composition, $Li_{1.18}Mn_{0.53}Ni_{0.21}Co_{0.08}O_2$. We used this target composition for all the calculations in the text.

**Electrochemical measurements.** All the samples that are not labelled as 'preformation' were first subjected to electrochemical cycling inside mini-18650 cells (Samsung) that contained a 92% LMR-NMC, 4% carbon and 4% binder composite by mass as the positive electrode and graphite as the negative electrode. The cells used a 1.3 M $LiPF_6$ in 3:8:9 (vol:vol:vol) fluoroethylene carbonate/hydrofluoroether/dimethyl carbonate electrolyte with some proprietary additives. This cycling included a four-cycle formation cycling procedure (Supplementary Methods) followed by cycling at 25 °C for the number of cycles specified in the text at a 1*C*/2*C* charge/discharge rate between 2.5 and 4.55 V with an about 45 min constant voltage held at 4.55 V until a *C*/20 current was reached. Note that each of these cycles also included a 10 min rest after both charging and discharging. *C* rates were calculated based on a capacity of 215 mAh $g^{-1}$. After the appropriate number of cycles was performed, the cells were then dismantled in a dry room. The electrodes harvested from these cells were then subjected to further electrochemical testing, as detailed below.

All the electrochemical tests shown in the text, other than the full-cell tests shown in Supplementary Fig. 1, were performed in 2032-type coin cells. A microbalance with a microgram level of accuracy (XPR2, Mettler Toledo) was used to mass the electrodes. They were assembled in an argon-filled glove box using lithium counter electrodes and 1 M $LiPF_6$ in an ethylene carbonate:diethyl carbonate (1:1 by weight) electrolyte (LP40, Gotion). They were electrochemically cycled using on a BCS-805 (Bio-logic) potentiostat at the current specified in the text. In Fig. 1a, the cycle numbers given are one higher than the number of cycles conducted in the mini-18650 cell (for example, the trace labelled cycle 46 underwent formation cycling, 45 normal charge–discharge cycles in the mini-18650 and then 1 more cycle at low a rate in a coin cell, which is shown). Note that in Fig. 1a, all the samples were cycled between 2.5 and 4.6 V other than the 2nd and 46th cycles, which were charged from 2 V, a negligible change given that less than 0.5 mAh $g^{-1}$ of capacity was observed between 2 and 2.5 V. The sample labelled 'preformation' in Supplementary Fig. 1 was directly fabricated into a 2032-type half-cell with no prior formation cycling and included a hold at 4.6 V for 9 mAh $g^{-1}$ of capacity to facilitate the 'activation' process. This sample was an 80% LMR-NMC, 10% carbon and 10% binder composite by mass. The second cycle data had a negligible hold of 3 mAh $g^{-1}$ at 4.6 V, and was excluded from the d*Q*/d*V* plot. We note that for the tests shown in Supplementary Fig. 54, a different cycling protocol was followed than that detailed above. The protocol is explained in detail in that figure.

**X-ray diffraction.** X-ray diffraction was performed at beamline 2-1 at the Stanford Synchrotron Radiation Lightsource (SSRL) at a 17 keV beam energy. A $LaB_6$ standard reference material was used to calibrate the energy. The capillaries were 0.5 mm special glass capillaries (Charles Supper) and were loaded inside an argon-filled glove box. The samples were rotated continuously throughout the measurement to avoid preferential orientation effects. The beam was 0.5 mm in width and 1 mm in height. Raw data were recorded using a Pilatus100K detector at a 700 mm distance from the capillary sample.

**X-ray absorption.** X-ray absorption was conducted in transmission mode on electrodes sealed under a pouch under argon at beamline 2-2 at SSRL. A Si(220) $\phi = 90°$ monochromator was used and was detuned to 50–60% of the maximum intensity to eliminate higher-order harmonics. The spectra of Ni, Co and Mn reference foils were used to calibrate the photon energy by setting the first crossing of zero of the second derivative of the absorbance spectrum to be 8,333, 7,709 and 6,539 eV, respectively. Three ion chambers were used in series to simultaneously measure $I_0$, $I_{sample}$ and $I_{ref}$. Spectrum normalization and alignment were performed using the Athena software package[70]. The samples shown in Supplementary Fig. 51 were measured at beamline 11-2 at SSRL with a similar set-up. EXAFS analysis and simulation were performed using the Artemis software package (Supplementary Methods)[70]. All the EXAFS data and simulations presented are based on $k^2$-weighted EXAFS spectra [$k^2\chi(k)$].

**Ultramicrotomy sample preparation.** Electrode-sized thin sections were prepared by removing the positive electrode from the coin-cell assembly using a coin-cell disassembling tool (Hohsen). Once removed, the positive electrode was dipped three times into a vial of dimethyl carbonate to remove any electrolyte or precipitated Li salts and allowed to dry for approximately 10 min. The dried electrodes were then cut into smaller pieces, typically into circular sectors. The cut electrodes were placed into a BEEM embedding capsules (size 0) with pointed end down. Subsequently, EpoFix, which is a low-viscosity epoxy, was poured into the capsule and all the remaining gas bubbles were removed from the capsule to ensure a uniform embedding of the sample and adequate penetration of the electrode pores. The epoxy was allowed to set for 24 h until hardened. Once hardened, the embedded samples were trimmed using a Leica Ultramicrotome UC7 equipped with a diamond trimming block (Diatome). The lateral size of the resulting block face was typically 150–200 µm square or rectangle. Once the block was shaped, sections were created using the Leica Ultramicrotome UC7 and a custom diamond knife (Diatome). The custom diamond knife was created specifically for dry sectioning of the embedded electrode sample, which removed the need for traditional water-based sample collection. The section thickness was normally set to a nominal one of 80 nm, although to prepare the samples shown in Supplementary Figs. 7, 25 and 26, the nominal thickness was set to 60 nm. During sectioning, a constant a.c. pulse was provided using a CRION antistatic device, to ensure that sections did not stick to the surface of the knife away from the edge. Sequential sections were collected using a gold-coated eyelash controlled using a micromanipulator, which utilized a static d.c. charge pulse, using the antistatic device, to attract the sections on to the eyelash. Once contacted, the eyelash was used to create a large ribbon that consisted of sequential sections by keeping the ribbon taut as new sections were cut. Once a sufficiently long ribbon was created, a second micromanipulator that held a TEM sample grid was brought into contact with the sample ribbon and then a d.c. pulse was used to detach the sample from the eyelash and attach it to the grid. From there, mesh grid samples were stored in a grid box inside a glove box until the X-ray microscopy measurements were performed. A reasonable agreement of the spatially averaged Mn oxidation state in the sectioned samples ($Mn^{3.80+}$ in Fig. 4a) with Mn oxidation states found from both K- and $L_3$-edge spectroscopy of non-sectioned samples (Fig. 1a and Supplementary Fig. 16) indicates that sectioning does not meaningfully alter the chemical state of the discharged electrodes. Likewise, the predominance of oxidized oxygen (Fig. 5c) in the sectioned charged samples[2,66,71] suggests that sectioning is unlikely to meaningfully alter the chemical state of the charged samples. Based on the qualitative similarities in, for example, Supplementary Figs. 26 and 27, it is likely that many primary particles remain intact after the ultramicrotomy process. Still, the cutting of some primary particles may occur and cannot be excluded. This sample preparation method was used for all the images of the material shown in the main text with the sole exception of the pristine particles in Fig. 2a.

**Dispersed sample preparation.** Samples prepared via sonication and dispersion were removed from the coin cells as above and then prepared as reported previously[2]. These samples account for the spectra in Fig. 1d (which are taken from the images shown in Supplementary Fig. 16) as well as the image of the pristine sample in Fig. 2a and all the samples in Supplementary Figs. 16, 17, 39, 41, 43, 44, 50 (pristine and $Mn_2O_3$) and 52.

**Scanning transmission X-ray microscopy.** Sectioned and dispersed samples were loaded onto 3 mm $Si_3N_4$ TEM grids (Norcada), with some measurements being taken on 3 mm copper TEM grids with a Formvar film coated with a layer of carbon (Ted Pella, mesh 100). The samples were transported sealed under argon to the ALS at the Lawrence Berkeley National Laboratory. STXM measurements were performed at beamlines 11.0.2.2 and 7.0.1.2 using a zone plate with an outer zone width of 45 nm. Images at different X-ray energies were aligned using the aXis2000 software package when possible and a custom Python script when necessary. The energy of the beam was calibrated at each edge using a reference sample, generally the pristine LMR material. Analysis was performed using custom MATLAB software.

**X-ray ptychography.** Ptychography measurements were performed at beamline 7.0.1.2 at the ALS and were taken almost exclusively in a double exposure mode to allow for maximum spatial resolution while avoiding detector saturation. The scan step size was set to ~40 nm, with a reconstructed image pixel size of ~5 nm. Supplementary Figs. 52 and 53 show that the samples' chemical states were not meaningfully altered by the high X-ray dose of the ptychography measurements.

**Scanning electron microscopy.** Samples for scanning electron microscopy were prepared by light sonication (~2 min) in isopropanol followed by being drop cast onto small sections of aluminium foil. Scanning electron micrographs were recorded on a Sirion SEM (FEI) at the Stanford Nano Shared Facilities.

**Inductively coupled plasma mass spectroscopy.** ICP-MS was performed on a Thermo Scientific XSERIES 2 ICP-MS at Stanford's Environmental Measurements Facility. Samples were prepared by washing with anhydrous dimethyl carbonate after cell disassembly, and then by dissolving the sample in 2% $HNO_3$ in the presence of ~1% $H_2O_2$. Although the carbon did not dissolve, the elemental composition found from an electrode was nearly identical to that found from the pristine material, which confirms the robustness of the preparation method. The quantity of each element present was found using a calibration curve generated by preparing seven standard solutions of known concentrations. Stock solutions of Li, Ni, Mn and Co dissolved in 2% $HNO_3$ (Inorganic Ventures) were used to prepare the standard solutions.

**Pycnometry.** Density measurements were conducted using a 1 $cm^3$ AccuPyc II 1340 automatic gas pycnometer (Micromeritics) with a 0.1 $cm^3$ insert and 99.9999% pure He gas (Praxair). The volumes of the insert and the expansion chamber were calibrated using a 0.718541 $cm^3$ standard ball bearing (Micromeritics). Ten or

more repeat measurements with cap removal and replacement were made of each sample, with the average and standard error reported in Fig. 3b.

**Neutron diffraction.** About 500 mg of pristine material was loaded in a 3 mm vanadium can, sealed under argon and transported to the POWGEN beamline at Oak Ridge National Laboratory. The diffraction pattern was then collected at room temperature in high-resolution mode using a beam of neutrons with a centre wavelength of 1.5 Å.

**Annealing of cycled electrodes.** The annealing of cycled electrodes was conducted by heating the cycled electrode, which was first discharged to and held at 2.5 V versus $Li/Li^+$ for ~6 h, and at 150 °C for 18 h in a 100% $O_2$ gas environment. The electrode did not delaminate during this process, and therefore the electrochemical test shown in Supplementary Fig. 31 was conducted simply by reassembling a coin cell with the electrode after heat treatment.

**Transmission electron microscopy.** Scanning TEM annular dark field images were taken using a FEI Titan Environment TEM operated at 300 kV with an image corrector. The probe size was 0.5 nm and the convergence and collection semi-angles were 9.3 mrad and 19–25 mrad, respectively. Selected area diffraction patterns were collected using the same TEM. High-resolution TEM images (Supplementary Figs. 8 and 9) were taken on a different TEM (FEI Tecnai G2 F20 X-TWIN), which was operated at an accelerating voltage of 200 kV.

**Focused ion beam sectioning.** For the TEM lamella prepared by sectioning with focused ion beam scanning electron microscopy, we used the FEI Helios 600i DualBeam FIB/SEM at the Stanford Nano Shared Facilities. Electron-beam and then ion-beam platinum deposition were performed sequentially to planarize the region to be extracted, at approximately 300 and 500 nm thicknesses each. Trench cuts were milled in front of and behind the protected region to expose the cross-section to be extracted. The lamella was polished down to about 1 µm thickness for extraction while at 30 kV and with the sample orthogonal to the ion beam. Reorienting the sample normal to the electron beam, a 'U'-cut was made cleanly through to define the edges of the lamella, with two tabs left at the top edges. An Omniprobe AutoProbe 200 standard tungsten tip was inserted and welded to one top corner using ion-beam deposited platinum. The lamella was then severed from the substrate and subsequently attached in a cantilever style to the edge of a copper Omniprobe lift-out grid post, also using ion-beam deposited platinum, and the needle was severed to release. The lamella was then further polished with the ion beam, both front and back, to a sub-200 nm thickness while at 30 kV and an additional ±1.5° tilt off-normal to strive for parallel sidewalls. Final polishing was done at 5 kV and a ±3° off-normal tilt to minimize amorphization damage and achieve electron transparency. This sample preparation method was used to create the images shown in Supplementary Figs. 8 and 9.

## Data availability

Data supporting the main text figures can be found at https://doi.org/10.5281/zenodo.4697951. Data supporting the Supplementary Information figures can be found at https://doi.org/10.5281/zenodo.4697955.

Received: 18 April 2020; Accepted: 19 April 2021;
Published online: 14 June 2021

## References

1. Croy, J. R., Balasubramanian, M., Gallagher, K. G. & Burrell, A. K. Review of the US Department of Energy's 'deep dive' effort to understand voltage fade in Li- and Mn-rich cathodes. *Acc. Chem. Res.* **48**, 2813–2821 (2015).
2. Gent, W. E. et al. Coupling between oxygen redox and cation migration explains unusual electrochemistry in lithium-rich layered oxides. *Nat. Commun.* **8**, 2091 (2017).
3. Sathiya, M. et al. Origin of voltage decay in high-capacity layered oxide electrodes. *Nat. Mater.* **14**, 230–238 (2015).
4. Abdellahi, A., Urban, A., Dacek, S. & Ceder, G. The effect of cation disorder on the average Li intercalation voltage of transition-metal oxides. *Chem. Mater.* **28**, 3659–3665 (2016).
5. Kleiner, K. et al. Origin of high capacity and poor cycling stability of Li-rich layered oxides—a long-duration in situ synchrotron powder diffraction study. *Chem. Mater.* **30**, 3656–3667 (2018).
6. Mohanty, D. et al. Unraveling the voltage-fade mechanism in high-energy-density lithium-ion batteries: origin of the tetrahedral cations for spinel conversion. *Chem. Mater.* **26**, 6272–6280 (2014).
7. Liu, H. et al. Unraveling the rapid performance decay of layered high-energy cathodes: from nanoscale degradation to drastic bulk evolution. *ACS Nano* **12**, 2708–2718 (2018).
8. Castel, E., Berg, E. J., El Kazzi, M., Novák, P. & Villevieille, C. Differential electrochemical mass spectrometry study of the interface of $xLi_2MnO_3{\cdot}(1-x)LiMO_2$ (M = Ni, Co, and Mn) material as a positive electrode in Li-ion batteries. *Chem. Mater.* **26**, 5051–5057 (2014).
9. Strehle, B. et al. The role of oxygen release from Li- and Mn-rich layered oxides during the first cycles investigated by on-line electrochemical mass spectrometry. *J. Electrochem. Soc.* **164**, A400–A406 (2017).
10. Hong, J. et al. Critical role of oxygen evolved from layered Li-excess metal oxides in lithium rechargeable batteries. *Chem. Mater.* **24**, 2692–2697 (2012).
11. Yan, P. et al. Injection of oxygen vacancies in the bulk lattice of layered cathodes. *Nat. Nanotechnol.* **14**, 602–608 (2019).
12. Hu, E. et al. Evolution of redox couples in Li- and Mn-rich cathode materials and mitigation of voltage fade by reducing oxygen release. *Nat. Energy* **3**, 690–698 (2018).
13. Wang, C. & Zhang, J. Structural and chemical evolution of Li- and Mn-rich layered cathode material. *Chem. Mater.* **27**, 1381–1390 (2015).
14. Zhu, Z. et al. Gradient Li-rich oxide cathode particles immunized against oxygen release by a molten salt treatment. *Nat. Energy* **4**, 1049–1058 (2019).
15. Gu, M. et al. Formation of the spinel phase in the layered composite cathode used in Li-ion batteries. *ACS Nano* **7**, 760–767 (2013).
16. Teufl, T., Strehle, B., Müller, P., Gasteiger, H. A. & Mendez, M. A. Oxygen release and surface degradation of Li- and Mn-rich layered oxides in variation of the $Li_2MnO_3$ content. *J. Electrochem. Soc.* **165**, A2718–A2731 (2018).
17. Qian, D., Xu, B., Chi, M. & Meng, Y. S. Uncovering the roles of oxygen vacancies in cation migration in lithium excess layered oxides. *Phys. Chem. Chem. Phys.* **16**, 14665–14668 (2014).
18. Mohanty, D. et al. Correlating cation ordering and voltage fade in a lithium–manganese-rich lithium-ion battery cathode oxide: a joint magnetic susceptibility and TEM study. *Phys. Chem. Chem. Phys.* **15**, 19496–19509 (2013).
19. Boulineau, A., Simonin, L., Colin, J. F., Bourbon, C. & Patoux, S. First evidence of manganese-nickel segregation and densification upon cycling in Li-rich layered oxides for lithium batteries. *Nano Lett.* **13**, 3857–3863 (2013).
20. Koga, H. et al. Reversible oxygen participation to the redox processes revealed for $Li_{1.20}Mn_{0.54}Co_{0.13}Ni_{0.13}O_2$. *J. Electrochem. Soc.* **160**, A786–A792 (2013).
21. Koga, H. et al. Different oxygen redox participation for bulk and surface: a possible global explanation for the cycling mechanism of $Li_{1.20}Mn_{0.54}Co_{0.13}Ni_{0.13}O_2$. *J. Power Sources* **236**, 250–258 (2013).
22. Gallagher, K. G. et al. Correlating hysteresis and voltage fade in lithium- and manganese-rich layered transition-metal oxide electrodes. *Electrochem. Commun.* **33**, 96–98 (2013).
23. Dau, H., Liebisch, P. & Haumann, M. X-ray absorption spectroscopy to analyze nuclear geometry and electronic structure of biological metal centers—potential and questions examined with special focus on the tetra-nuclear manganese complex of oxygenic photosynthesis. *Anal. Bioanal. Chem.* **376**, 562–583 (2003).
24. Yabuuchi, N., Yoshii, K., Myung, S.-T., Nakai, I. & Komaba, S. Detailed studies of a high-capacity electrode material for rechargeable batteries, $Li_2MnO_3$–$LiCo_{1/3}Ni_{1/3}Mn_{1/3}O_2$. *J. Am. Chem. Soc.* **133**, 4404–4419 (2011).
25. Luo, K. et al. Charge-compensation in 3*d*-transition-metal-oxide intercalation cathodes through the generation of localized electron holes on oxygen. *Nat. Chem.* **8**, 684–691 (2016).
26. Lee, J. et al. Mitigating oxygen loss to improve the cycling performance of high capacity cation-disordered cathode materials. *Nat. Commun.* **8**, 981 (2017).
27. Bluhm, H. et al. Soft X-ray microscopy and spectroscopy at the molecular environmental science beamline at the Advanced Light Source. *J. Electron Spectros. Relat. Phenom.* **150**, 86–104 (2006).
28. Celestre, R. et al. Nanosurveyor 2: A compact Instrument for nano-tomography at the Advanced Light Source. *J. Phys. Conf. Ser.* **849**, 6–10 (2017).
29. Yu, Y. S. et al. Dependence on crystal size of the nanoscale chemical phase distribution and fracture in $Li_xFePO_4$. *Nano Lett.* **15**, 4282–4288 (2015).
30. Shapiro, D. A. et al. Chemical composition mapping with nanometre resolution by soft X-ray microscopy. *Nat. Photon.* **8**, 765–769 (2014).
31. Hong, J. et al. Metal–oxygen decoordination stabilizes anion redox in Li-rich oxides. *Nat. Mater.* **18**, 256–265 (2019).
32. Yang, F. et al. Nanoscale morphological and chemical changes of high voltage lithium–manganese rich NMC composite cathodes with cycling. *Nano Lett.* **14**, 4334–4341 (2014).
33. Genevois, C. et al. Insight into the atomic structure of cycled lithium-rich layered oxide $Li_{1.20}Mn_{0.54}Co_{0.13}Ni_{0.13}O_2$ using HAADF STEM and electron nanodiffraction. *J. Phys. Chem. C* **119**, 75–83 (2015).
34. Li, J., Shunmugasundaram, R., Doig, R. & Dahn, J. R. In situ X-ray diffraction study of layered Li–Ni–Mn–Co oxides: effect of particle size and structural stability of core–shell materials. *Chem. Mater.* **28**, 162–171 (2016).
35. Huang, Y. et al. Thermal stability and reactivity of cathode materials for Li-ion batteries. *ACS Appl. Mater. Interfaces* **8**, 7013–7021 (2016).
36. Bak, S. M. et al. Structural changes and thermal stability of charged $LiNi_xMn_yCo_zO_2$ cathode materials studied by combined in situ time-resolved XRD and mass spectroscopy. *ACS Appl. Mater. Interfaces* **6**, 22594–22601 (2014).
37. Nemudry, A., Goldberg, E. L., Aguirre, M. & Alario-Franco, M. Á. Electrochemical topotactic oxidation of nonstoichiometric perovskites at ambient temperature. *Solid State Sci.* **4**, 677–690 (2002).

38. Mefford, J. T. et al. Water electrolysis on $La_{1-x}Sr_xCoO_{3-\delta}$ perovskite electrocatalysts. *Nat. Commun.* **7**, 11053 (2016).
39. Mefford, J. T., Hardin, W. G., Dai, S., Johnston, K. P. & Stevenson, K. J. Anion charge storage through oxygen intercalation in $LaMnO_3$ perovskite pseudocapacitor electrodes. *Nat. Mater.* **13**, 726–732 (2014).
40. Kudo, T., Obayashi, H. & Gejo, T. Electrochemical behavior of the perovskite-type $Nd_{1-x}Sr_xCoO_3$ in an aqueous alkaline solution. *J. Electrochem. Soc.* **122**, 159–163 (1975).
41. House, R. A. et al. First-cycle voltage hysteresis in Li-rich 3*d* cathodes associated with molecular $O_2$ trapped in the bulk. *Nat. Energy* **5**, 777–785 (2020).
42. Lee, E. & Persson, K. A. Structural and chemical evolution of the layered Li-excess $Li_xMnO_3$ as a function of Li content from first-principles calculations. *Adv. Energy Mater.* **4**, 1400498 (2014).
43. Gerbig, O., Merkle, R. & Maier, J. Electrical transport and oxygen exchange in the superoxides of potassium, rubidium, and cesium. *Adv. Funct. Mater.* **25**, 2552–2563 (2015).
44. Royer, S., Duprez, D. & Kaliaguine, S. Oxygen mobility in $LaCoO_3$ perovskites. *Catal. Today* **112**, 99–102 (2006).
45. Singer, A. et al. Nucleation of dislocations and their dynamics in layered oxide cathode materials during battery charging. *Nat. Energy* **3**, 641–647 (2018).
46. Tran, N. et al. Mechanisms associated with the 'plateau' observed at high voltage for the overlithiated $Li_{1.12}(Ni_{0.425}Mn_{0.425}Co_{0.15})_{0.88}O_2$ system. *Chem. Mater.* **20**, 4815–4825 (2008).
47. Armstrong, A. R. et al. Demonstrating oxygen loss and associated structural reorganization in the lithium battery cathode $Li[Ni_{0.2}Li_{0.2}Mn_{0.6}]O_2$. *J. Am. Chem. Soc.* **128**, 8694–8698 (2006).
48. Wu, Y. & Manthiram, A. Effect of surface modifications on the layered solid solution cathodes $(1-z)\ Li[Li_{1/3}Mn_{2/3}]O_2 - (z)\ Li[Mn_{0.5-y}Ni_{0.5-y}Co_{2y}]O_2$. *Solid State Ion.* **180**, 50–56 (2009).
49. Yin, W. et al. Structural evolution at the oxidative and reductive limits in the first electrochemical cycle of $Li_{1.2}Ni_{0.13}Mn_{0.54}Co_{0.13}O_2$. *Nat. Commun.* **11**, 1252 (2020).
50. Zhang, Z. et al. Cathode–electrolyte interphase in lithium batteries revealed by cryogenic electron microscopy. *Matter* **4**, 302–312 (2021).
51. Shunmugasundaram, R., Senthil Arumugam, R. & Dahn, J. R. High capacity Li-rich positive electrode materials with reduced first-cycle irreversible capacity loss. *Chem. Mater.* **27**, 757–767 (2015).
52. Qiu, B. et al. Metastability and reversibility of anionic redox-based cathode for high-energy rechargeable batteries. *Cell Rep. Phys. Sci.* **1**, 100028 (2020).
53. Xu, B., Fell, C. R., Chi, M. & Meng, Y. S. Identifying surface structural changes in layered Li-excess nickel manganese oxides in high voltage lithium ion batteries: a joint experimental and theoretical study. *Energy Environ. Sci.* **4**, 2223–2233 (2011).
54. Lin, F. et al. Surface reconstruction and chemical evolution of stoichiometric layered cathode materials for lithium-ion batteries. *Nat. Commun.* **5**, 3529 (2014).
55. Fell, C. R. et al. Correlation between oxygen vacancy, microstrain, and cation distribution in lithium-excess layered oxides during the first electrochemical cycle. *Chem. Mater.* **25**, 1621–1629 (2013).
56. Zheng, J. et al. Functioning mechanism of $AlF_3$ coating on the Li- and Mn-rich cathode materials. *Chem. Mater.* **26**, 6320–6327 (2014).
57. Mohanty, D. et al. Modification of Ni-rich FCG NMC and NCA cathodes by atomic layer deposition: preventing surface phase transitions for high-voltage lithium-ion batteries. *Sci. Rep.* **6**, 26532 (2016).
58. Mortemard de Boisse, B. et al. Highly reversible oxygen-redox chemistry at 4.1 V in $Na_{4/7-x}[\square_{1/7}Mn_{6/7}]O_2$ ($\square$: Mn vacancy). *Adv. Energy Mater.* **8**, 1800409 (2018).
59. Eum, D. et al. Voltage decay and redox asymmetry mitigation by reversible cation migration in lithium-rich layered oxide electrodes. *Nat. Mater.* **19**, 419–428 (2020).
60. Maitra, U. et al. Oxygen redox chemistry without excess alkali-metal ions in $Na_{2/3}[Mg_{0.28}Mn_{0.72}]O_2$. *Nat. Chem.* **10**, 288–295 (2018).
61. House, R. A. et al. Superstructure control of first-cycle voltage hysteresis in oxygen-redox cathodes. *Nature* **577**, 502–508 (2019).
62. Gent, W. E. et al. Persistent state-of-charge heterogeneity in relaxed, partially charged $Li_{1-x}Ni_{1/3}Co_{1/3}Mn_{1/3}O_2$ secondary particles. *Adv. Mater.* **28**, 6631–6638 (2016).
63. Liu, J. et al. Electrochemical performance studies of Li-rich cathode materials with different primary particle sizes. *J. Power Sources* **251**, 208–214 (2014).
64. Ruess, R. et al. Influence of NCM particle cracking on kinetics of lithium-ion batteries with liquid or solid electrolyte. *J. Electrochem. Soc.* **167**, 100532 (2020).
65. Li, J. et al. Comparison of single crystal and polycrystalline $LiNi_{0.5}Mn_{0.3}Co_{0.2}O_2$ positive electrode materials for high voltage Li-ion cells. *J. Electrochem. Soc.* **164**, A1534–A1544 (2017).
66. Assat, G., Iadecola, A., Foix, D., Dedryvère, R. & Tarascon, J.-M. Direct quantification of anionic redox over long cycling of Li-rich NMC via hard X-ray photoemission spectroscopy. *ACS Energy Lett.* **3**, 2721–2728 (2018).
67. Qiu, B. et al. Gas-solid interfacial modification of oxygen activity in layered oxide cathodes for lithium-ion batteries. *Nat. Commun.* **7**, 12108 (2016).
68. Kim, S., Cho, W., Zhang, X., Oshima, Y. & Choi, J. W. A stable lithium-rich surface structure for lithium-rich layered cathode materials. *Nat. Commun.* **7**, 13598 (2016).
69. Lu, Z. & Dahn, J. R. In situ X-ray diffraction study of $P2\text{-}Na_{2/3}[Ni_{1/3}Mn_{2/3}]O_2$. *J. Electrochem. Soc.* **148**, A1225 (2001).
70. Ravel, B. & Newville, M. ATHENA, ARTEMIS, HEPHAESTUS: data analysis for X-ray absorption spectroscopy using IFEFFIT. *J. Synchrotron Radiat.* **12**, 537–541 (2005).
71. Dai, K. et al. High reversibility of lattice oxygen redox quantified by direct bulk probes of both anionic and cationic redox reactions. *Joule* **3**, 518–541 (2018).


## Acknowledgements

The battery component of this work was supported by the Assistant Secretary for Energy Efficiency and Renewable Energy, Office of Vehicle Technologies, Battery Materials Research Program, US Department of Energy (DOE), and by Samsung Advanced Institute of Technology Global Research Outreach program. STXM and X-ray ptychography development was supported by the DOE, Office of Basic Energy Sciences, Division of Materials Sciences and Engineering (contract DE-AC02-76SF00515). This research used resources of the ALS, a DOE Office of Science User Facility under contract no. DE-AC02-05CH11231. This work was partially supported by STROBE, a National Science Foundation Science and Technology Center under award DMR1548924. Use of the SSRL, SLAC National Accelerator Laboratory, is supported by the US Department of Energy, Office of Science, Office of Basic Energy Sciences under contract no. DE-AC02-76SF00515. A portion of this research used resources at the Spallation Neutron Source, a DOE Office of Science User Facility operated by the Oak Ridge National Laboratory. Part of this work was performed at the Stanford Nano Shared Facilities, supported by the National Science Foundation under award ECCS-1542152. P.M.C. acknowledges support through the Stanford Graduate Fellowship as a Winston and Fu-Mei Chen fellow and through the National Science Foundation Graduate Research Fellowship under Grant no. DGE-1656518. W.E.G. was supported additionally by the ALS Doctoral Fellowship. Y.L. and R.S. acknowledge the financial support from the Toyota Research Institute—Accelerated Materials Design and Discovery (TRI-AMDD) program (Stanford University). We thank L. Echávez, L. Schelhas, T. Mefford, M. Lattimer and B. Enders for helpful discussions and/or experimental support. We acknowledge R. Chin for performing the FIB electrode cross-sectioning for the TEM experiments. We also acknowledge R. Kim for experimental TEM support and helpful discussions.

## Author contributions

P.M.C., S.S.K., W.E.G., D.A.S., M.F.T. and W.C.C. conceived the study. S.S.K. and E.K. performed the ultramicrotomy sectioning. P.M.C., S.S.K., W.E.G., Y.-S.Y. and D.A.S. collected ex situ STXM and ptychography images and analysed the data. P.M.C., K.L. and K.H.S. collected the SXRD data. P.M.C. collected the neutron diffraction data. P.M.C., K.L., K.H.S. and M.F.T. analysed the diffraction data. S.-J.A. synthesized the material and cycled the mini-18650 cells. P.M.C. performed the ICP-MS, scanning electron microscopy and pycnometry experiments. P.M.C. collected TM K-edge spectra and K.L., W.E.G. and M.F.T. contributed to the interpretation. P.M.C. and W.C.C. developed the diffusion and two-phase core–shell models used. Y.L. and X.X. collected TEM images. Y.L., X.X., P.M.C., A.F.M., R.S. and W.C.C. analysed the TEM data. P.M.C, W.C.C. and M.F.T. wrote the manuscript and all the authors revised the manuscript.

## Competing interests

The authors declare no competing interests.

## Additional information

**Supplementary information** The online version contains supplementary material available at https://doi.org/10.1038/s41560-021-00832-7.

**Correspondence and requests for materials** should be addressed to D.A.S., M.F.T. or W.C.C.

**Peer review information** *Nature Energy* thanks the anonymous reviewers for their contribution to the peer review of this work.

**Reprints and permissions information** is available at www.nature.com/reprints.

**Publisher's note** Springer Nature remains neutral with regard to jurisdictional claims in published maps and institutional affiliations.